



## Enhanced ceria nanoflakes using graphene oxide as a sacrificial template for CO oxidation and dry reforming of methane

Shawn C. Rood<sup>a,b</sup>, Huseyin B. Ahmet<sup>c</sup>, Anais Gomez-Ramon<sup>d</sup>, Laura Torrente-Murciano<sup>e</sup>, Tomas R. Reina<sup>c</sup>, Salvador Eslava<sup>b,\*</sup>

<sup>a</sup> Centre for Doctoral Training in Sustainable Chemical Technologies, University of Bath, Claverton Down, Bath, BA2 7AY, UK

<sup>b</sup> Department of Chemical Engineering, University of Bath, Claverton Down, Bath, BA2 7AY, UK

<sup>c</sup> Department of Chemical Engineering, University of Surrey, Guilford, GU2 7XH, UK

<sup>d</sup> Departament d'Enginyeria Química, Biològica i Ambiental, Universitat Autònoma de Barcelona, Bellaterra, 08193, Spain

<sup>e</sup> Department of Chemical Engineering and Biotechnology, University of Cambridge, Philippa Fawcett Drive, Cambridge, CB3 0AS, UK

### ARTICLE INFO

#### Keywords:

Ceria  
Dry methane reforming  
CO oxidation  
Graphene oxide  
Template

### ABSTRACT

The development of novel fabrication methods to produce ceria catalysts with good high-temperature stability is critical for their implementation across a range of different applications. Herein, graphene oxide flakes are used as a sacrificial template in the synthesis of ceria particles to replicate the graphene oxide's two-dimensionality. While performing the synthesis without graphene oxide results in large agglomerations of ceria crystallites, the addition of graphene oxide during the synthesis results in ceria nanoflakes (< 10 nm) replicating the graphene oxide morphology. This novel shape limits the diffusion of atoms at high temperature to a two-dimensional plane which is translated into a low sintering degree and consequently, an enhanced thermal stability. In this way, the ceria flakes are capable of maintaining high surface areas after calcination at high temperatures (> 400 °C) which results in improved catalytic performance for the oxidation of carbon monoxide. This resistance versus sintering has also a beneficial effect when ceria flakes are used as catalytic support of nickel particles. Improved metal dispersion and high metal-support interaction leads to lower sintering during the dry reforming of methane than similarly prepared un-templated ceria nickel catalysts. These results demonstrate the advantage of using graphene oxide as a sacrificial template for the production of sintering-resistant catalysts with good catalytic performance at high temperatures.

### 1. Introduction

Ceria-based materials are well-known for their use as a catalyst or catalyst support in a variety of environmentally sensitive applications, including automotive catalysis, VOC oxidation, solid oxide fuel cells, steam reformation for hydrogen production, photocatalysis, and thermochemical water splitting [1–8]. Ceria's ability to easily cycle between 4+ and 3+ oxidation states allows it to act as an oxygen storage medium - for example, storing and releasing oxygen in response to the varying air-to-fuel ratio in a vehicle's exhaust to optimize catalytic converter performance [9]. Ceria has also been utilized as a catalyst support or promoter in the dry reforming of methane (DRM) for syngas production, where it enhances activity [10,11]. The use of ceria in DRM as a catalyst support for nickel, instead of other supports such as Al<sub>2</sub>O<sub>3</sub> or SiO<sub>2</sub>, also inhibits coke formation, otherwise a significant source of

deactivation in this reaction [12,13]. Recently, ceria's redox cycle has been utilized in the thermochemical splitting of water, using concentrated solar energy to reduce cerium ions to Ce<sup>3+</sup> at high temperatures, followed by reoxidation with water molecules to produce hydrogen, syngas, or hydrocarbons [5,14]. Another recent application for ceria is roomtemperature dehydrogenation of formic acid, where it demonstrated greatly improved activity compared with other supports [15]. Ceria morphology at the nanoscale has also been shown to have an effect on the olefin selectivity on the CO<sub>2</sub> hydrogenation reaction to hydrocarbons [16].

Many ceria applications involve heterogeneous surface-catalyzed reactions, so the ability to synthesize high surface area ceria is critical to improve performance. Surface areas over 200 m<sup>2</sup> g<sup>-1</sup> are often reported for nanostructured ceria materials synthesized via a variety of methods such as hydrothermal or sol-gel, and surface areas of

Abbreviations: GO, graphene oxide

\* Corresponding author.

E-mail address: [s.eslava@bath.ac.uk](mailto:s.eslava@bath.ac.uk) (S. Eslava).

<https://doi.org/10.1016/j.apcatb.2018.10.011>

Received 29 June 2018; Received in revised form 2 October 2018; Accepted 6 October 2018

Available online 09 October 2018

0926-3373/ © 2018 The Authors. Published by Elsevier B.V. This is an open access article under the CC BY license

(<http://creativecommons.org/licenses/by/4.0/>).

$345 \text{ m}^2 \text{ g}^{-1}$  has been obtained in ceria aerogel materials [17–19]. The morphology of nanoceria and the nature of its exposed crystal planes can also affect catalytic activity [6,20–22]. However, in numerous applications, ceria must also present a high thermal stability to maintain a useable surface area even when exposed to high temperatures. The next generation of low-temperature solid oxide fuel cells still have a temperature range of up to  $650 \text{ }^\circ\text{C}$ , while the ceria reduction step in thermochemical water splitting generally involves temperatures greater than  $1200 \text{ }^\circ\text{C}$ . Automotive catalysts can be exposed to vehicle exhaust temperatures of  $850 \text{ }^\circ\text{C}$ , and close-coupled automotive catalysts can reach  $1050 \text{ }^\circ\text{C}$  [23,24]. Dry reformation of methane often requires temperatures in excess of  $800 \text{ }^\circ\text{C}$  due to the highly endothermic nature of the reaction [25,26].

To synthesize nanostructured ceria of various morphologies, numerous templating agents have been reported, such as metal-organic frameworks and carbon microspheres [20,27,28]. Carbon nanotubes, ZnO nanotubes, and Ag nanowires have been used as templates to synthesize ceria nanotubes, while polystyrene and silica spheres have been used to synthesize hollow ceria nanospheres [29–33]. However, these methods often involve either an additional chemical treatment step to remove the template and full removal is usually difficult to achieve.

The use of graphene oxide (GO) as a template offers an attractive alternative route for synthesizing high surface area nanostructured ceria catalysts. GO consists of a two-dimensional monolayer of carbon atoms, analogous to graphene, but interrupted by a range of oxygen-containing groups [34].

GO's surface functional oxygen-containing groups allow it to be easily dispersed in a variety of solvents, unlike graphene, enabling its utilization in processes involving liquid suspensions or solutions [35]. The use of GO as a templating agent allows its two-dimensional structure to be replicated. For instance, the synthesis of manganese oxide nanoflakes has been reported by mixing a potassium permanganate solution into a suspension of GO, resulting in the in situ replacement of carbon atoms with manganese [36]. Titanium oxide nanoflakes have been synthesized by anchoring  $\text{Ti}_{16}\text{O}_{16}(\text{OEt})_{32}$  clusters onto GO suspended in tetrahydrofuran, followed by calcination at  $450 \text{ }^\circ\text{C}$  to decompose the GO, which resulted in a two-dimensional titania structure replicating the GO shape [34].

In this work, the use of GO as a sacrificial template for the synthesis of ceria nanoflakes via a precipitation reaction is reported. It is shown that a highly two-dimensional structure is achieved. Due to improved textural properties, these ceria nanoflakes demonstrate better anti-sintering behavior and higher catalytic activity compared with untemplated ceria particles produced in a GO-free precipitation synthesis. The catalytic activity of both materials (templated and untemplated) is tested for CO oxidation for eventual application in automotive catalysis. The use of templated ceria flakes as a catalyst support for nickel nanoparticles in dry reformation of methane (DRM) is also examined. In both cases, the flakes offer enhanced catalytic activity compared with untemplated ceria particles. Templating ceria with GO offers a potential way for the synthesis of catalysts with better performance for high-temperature applications such as automotive catalysis or dry reforming of methane.

## 2. Experimental

GO was prepared by oxidizing and exfoliating graphite with a modified Tour et al. synthesis method [34,37]. 24 g of 100–500  $\mu\text{m}$  natural graphite flakes (Aldrich) were added to a concentrated acid mixture (3 L  $\text{H}_2\text{SO}_4$  : 0.3 L  $\text{H}_3\text{PO}_4$ ) under vigorous stirring. 144 g of  $\text{KMnO}_4$  was added gradually. The reaction mixture was vigorously stirred for 18 h at  $50 \text{ }^\circ\text{C}$ . Next, the mixture was cooled to room temperature and 1.72 L of 2 wt. % aqueous  $\text{H}_2\text{O}_2$  was added dropwise to stop the oxidation reactions. The resulting suspension of GO was washed by repeated centrifugation and re-dispersion in distilled water

until the pH of the supernatant matched that of the original distilled water (typically after 16 washing cycles). Then, un-exfoliated graphite particles were separated with two further low-speed ( $< 1000 \text{ rpm}$ ) centrifugation cycles. Finally, the GO suspension was freeze-dried at  $-60 \text{ }^\circ\text{C}$  and stored at room temperature.

Ceria nanoflakes were prepared using a room temperature precipitation reaction [38]. A suspension of GO in deionized water (3 wt. %) was prepared. 3 mL of this 3 wt. % GO suspension in water was added to 600 mL of deionized water, and aqueous ammonia solution (30%) was added to adjust the pH to 11.0. 150 mL of 0.05 mol L<sup>-1</sup> cerium nitrate in deionized water was added dropwise to the GO/ammonia solution under stirring. The solution was left to stir for 3 h under ambient conditions. Next, three cycles of centrifugation (4000 rpm for 10 min) and redispersion in distilled water were performed to wash the product. The wet powder was freeze-dried at  $-60 \text{ }^\circ\text{C}$ . Untemplated ceria particles were prepared using the same procedure, without the addition of GO prior to pH adjustment.

After synthesis, the product was calcined at  $400 \text{ }^\circ\text{C}$  for 3 h to remove the GO. For CO oxidation experiments and characterization, different samples were prepared by further calcination undertaken at 600, 800, 900, and  $1000 \text{ }^\circ\text{C}$  for 3 h. Calcination was performed in air under static conditions.

For dry reformation of methane, the ceria catalysts calcined at  $400 \text{ }^\circ\text{C}$  were dispersed in ethanol with a corresponding amount of Ni ( $\text{NO}_3$ )<sub>2</sub>·6H<sub>2</sub>O to achieve a loading of 10 wt. % Ni. After stirring for 30 min, the solvent was removed by drying under vacuum in a rotary evaporator. The product was further dried in an oven overnight at  $80 \text{ }^\circ\text{C}$ . Finally, the dried powder was calcined at  $700 \text{ }^\circ\text{C}$  for 4 h in air under static conditions.

Powder x-ray diffraction (XRD) was performed with either a Bruker D8-Advance or X'Pert Pro PANalytical instrument using Cu K $\alpha$  radiation. Samples were measured in the 2 theta range of  $20\text{--}90^\circ$  with a step size of  $0.0164^\circ$  and 0.25 s per step, or  $5\text{--}80^\circ$  with a step size of  $0.05^\circ$  and step time of 0.16 s per step. Crystallite size was calculated using the Scherrer equation and the unit cell parameter was calculated using Bragg's law. Nitrogen adsorption experiments were performed with a Micromeritics 3Flex Surface Characterization Analyzer. Samples were degassed under vacuum at  $200 \text{ }^\circ\text{C}$  for 90 min. Specific surface areas were calculated using the Brunauer-Emmett-Teller (BET) method and pore size was calculated using the Barrett-Joyner-Halenda (BJH) method on the desorption curves.

Temperature-programmed reduction was performed with a Micromeritics AutoChem II 2920. 0.1 g of each sample was heated under  $50 \text{ mL min}^{-1}$  of 5%  $\text{H}_2$  in argon to  $900 \text{ }^\circ\text{C}$  at a rate of  $10 \text{ }^\circ\text{C min}^{-1}$ . The outlet gas was analyzed to quantify the amount of hydrogen consumed with a thermal conductivity detector. Scanning electron microscopy (SEM) was performed with an LEO 1525 field emission gun scanning electron microscope. Transmission electron microscopy (TEM) was performed with a JEOL JEM1200EXII or JEOL JEM-2100Plus microscope. EDX analysis was performed with an Oxford Instruments large area EDX detector integrated into the TEM. Raman analysis was performed with a Renishaw inVia Raman Microscope. A 532 nm green laser was used, and spectra were obtained with 2–10 s exposure time at 1–10% laser power. Thermogravimetric analysis (TGA) after the DRM reactions was carried out in a TA Instruments Discovery TGA, Q50. Approximately 3 mg of sample was combusted under  $40 \text{ mL min}^{-1}$  of air flow from  $50$  to  $900 \text{ }^\circ\text{C}$  at  $10 \text{ }^\circ\text{C min}^{-1}$ .

Catalytic activity tests for CO oxidation were performed in a U-shaped quartz tube reactor (10 mm ID) at atmospheric pressure. In a typical experiment, 10 mg of ceria catalyst was dispersed in a  $4 \text{ cm}^3$  catalytic bed consisting of silicon carbide particles. The catalytic bed was secured at both ends with quartz wool. The reactant feed consisted of 2000 ppm each CO and  $\text{O}_2$  in nitrogen, with a total flow rate of  $50 \text{ mL min}^{-1}$ , achieving a weight hourly space velocity (WHSV) of  $300 \text{ L g}^{-1} \text{ h}^{-1}$ . The catalyst was tested from room temperature to  $500 \text{ }^\circ\text{C}$ , and the outlet gas was measured with a Fuji Electric ZRH Infrared Gas Analyzer

and a Hitachi mass spectrometer. Statistical analysis: each data point reported for CO oxidation represents the average of ten continuously logged data points during testing. Therefore, error bars reported in Fig. 7 show instrument error.

Catalytic activity tests for the dry reforming of methane were performed in a tubular quartz reactor (10 mm ID) at atmospheric pressure. Catalysts were reduced in H<sub>2</sub> atmosphere (10 vol. % H<sub>2</sub> balanced in N<sub>2</sub>) at 850 °C for 1 h prior to the activity tests. In a typical experiment, 100 mg of Ni-ceria catalyst was loaded in the reactor, supported on a bed of quartz wool. The reactant feed consisted of a 1/1/6 ratio of CH<sub>4</sub>/CO<sub>2</sub>/N<sub>2</sub>, with a total flow rate of 100 mL min<sup>-1</sup>, achieving a WHSV of 60 L g<sup>-1</sup> h<sup>-1</sup>. Reactants and products were monitored using an on-line gas analyzer (ABB AO2020), equipped with both IR and TCD detectors. The catalyst was tested between 550 and 850 °C. Long-term dry reforming studies were performed at a constant temperature of 800 °C for 20 h.

### 3. Results and discussion

Ceria particles and nanoflakes were prepared via a room temperature precipitation synthesis in the absence and presence of GO respectively, followed by a calcination in air at 400 °C to remove the GO template. An SEM micrograph of the GO used is shown in Fig. 1. Prior to calcination, the nanoflakes are a brown powder, while after calcination at 400 °C, the product is yellow, similar to other ceria syntheses (Fig. S1). The untemplated ceria particles were bright yellow both pre- and post-calcination. The GO-templated ceria nanoflakes were much more loosely packed than the untemplated ceria particles. Without any further treatment, the nanoflakes had a bulk density of 0.34 g mL<sup>-1</sup>, while the untemplated particles had a bulk density of 0.65 g mL<sup>-1</sup>.

Fig. 2 shows TEM images of GO-templated ceria nanoflakes and untemplated ceria particles calcined in air at different temperatures between 400–1000 °C. The difference between the two materials is significant - while the GO-templated synthesis provided a two-dimensional arrangement of ceria crystallites, the untemplated synthesis resulted in much larger unstructured agglomerations. Typical ceria flakes calcined at 400 °C were a few hundred nanometers in diameter and less than 10 nm in thickness, while the size of the untemplated ceria particle agglomerations was significantly larger, in the micrometer range.

Subsequent calcinations in air at 600, 800, 900, or 1000 °C to assess thermal stability also show differences between GO-templated ceria flakes and untemplated ceria particles. While both the ceria nanoflakes and particles show crystallite growth with increasing calcination temperature, the ceria nanoflakes retained their two-dimensional morphology even at high calcination temperatures (1000 °C).

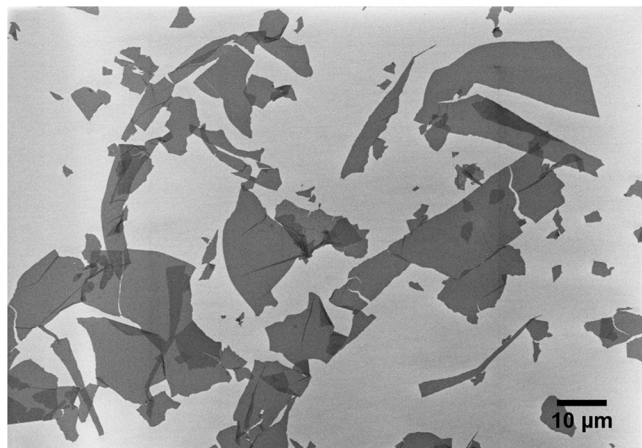


Fig. 1. SEM micrograph of graphene oxide used as the template for ceria nanoflakes synthesis. The size distribution of GO flakes was approximately 1–20 μm.

Powder XRD patterns of the calcined ceria particles and nanoflakes crystallite sizes show that both are very similar. Fig. 3 shows that the diffraction peaks get narrower and taller with increasing calcination temperature, indicating a growth in crystallite size. However, this trend is more prominent for the untemplated ceria particles compared to the GO-templated ceria nanoflakes for any calcination temperature. Crystallite size calculations using the ceria (111) peaks clearly show this trend in Table 1. When calcined at 400 °C, the ceria particles and flakes have a similar crystallite size, slightly smaller for the flakes (6.7 and 6.0 nm, respectively). But upon calcination at higher temperatures, crystallite size increases more quickly for the untemplated particles than for the GO-templated nanoflakes. This observation indicates that the two dimensional high aspect ratio arrangement of crystallites of the GO-templated nanoflakes replicating the GO morphology limits the diffusion of atoms at high temperature to a two dimensional plane which is translated into a low sintering degree. In contrast, diffusion of atoms at high temperature in untemplated particles takes place in three dimensions, favoring the sintering.

CHN analysis indicates that the GO is eliminated from the templated ceria material after the initial calcination at 400 °C. Pre-calcination, the ceria flakes and untemplated ceria particles contain 1.64 and 0.38 wt. % carbon, respectively, confirming the presence of GO. After calcination at 400 °C, the ceria flakes and untemplated ceria particles contain 0.39 and 0.34 wt. % carbon, respectively. These comparable values confirm the volatilization of GO during the calcination in air at 400 °C. Visual analysis of the materials support this - before calcination, the GO-templated ceria flakes are dark brown, but after calcination, they are pale yellow, more typical for ceria powders (Fig. S1). Numerous examples of GO-ceria composite materials have been reported in the literature. For instance, hydrothermal methods have been used to synthesize ceria nanoparticles dispersed on the surface of graphene oxide for the oxidation of uric acid, degradation of methylene blue, and removal of arsenic species from water [39–41]. However, because calcination at 400 °C is sufficient to completely remove GO from such composite materials, there is quite a low upper temperature limit for such catalysts to be useful. In contrast, the GO-templated ceria flakes retain useful properties at much higher temperatures.

Both the ceria particles and templated flakes were analyzed with Raman spectroscopy, shown in Fig. 4. In both cases, ceria's characteristic F<sub>2g</sub> band at approximately 466 cm<sup>-1</sup>, attributable to the vibrational characteristics of oxygen atoms surrounding cerium in the fluorite crystal structure, is clearly visible [42]. An additional defect band at 595 cm<sup>-1</sup> is also visible in both samples calcined at 400 °C. This defect band can be attributed to the presence of Ce<sup>3+</sup> related defects in the ceria lattice, or to defects caused by crystallite size effects - in general, in pure ceria it can be related to oxygen vacancy concentration due to non-stoichiometry of the CeO<sub>2</sub> lattice [43,44]. Shifts in the 466 cm<sup>-1</sup> band can be attributed to differences in oxygen vacancy levels or lattice contraction, and this would also be indicated in a difference in intensity in the 595 cm<sup>-1</sup> band [45–47]. While the GO templated and untemplated samples calcined at 400 °C appear to be similar, the 595 cm<sup>-1</sup> band disappears in the untemplated ceria particle spectrum at calcination temperatures > 600 °C, while it is retained in the GO-templated ceria spectrum even after treatments at 1000 °C, although its magnitude is considerably decreased.

Oxygen vacancy quantities can be calculated via correlation with a shift in the main F<sub>2g</sub> band at ~466 cm<sup>-1</sup> [48,49]. Results are shown in Table 1. For pure ceria,  $\Delta\omega = -\gamma\omega/(\Delta V/V_0)$ , where  $\omega$  is the shift in Raman frequency,  $\gamma$  is the Grüneisen parameter (1.24 for this mode), and  $\Delta V$  is the volume change from the reference volume. Volume changes of the unit cell are due to expansion of Ce<sup>4+</sup> to Ce<sup>3+</sup> (ionic radii 0.970 Å and 1.143 Å, respectively), which is only partially offset by the replacement of O<sup>2-</sup> with oxygen vacancies (ionic radii 1.380 and 1.164 Å, respectively). Assuming pure ceria with no other contributing defects, the relationship between oxygen vacancy concentration  $\delta$  and change in volume  $\Delta V/V_0$  is relatively linear:  $\delta = -10(\Delta a/a_0) =$

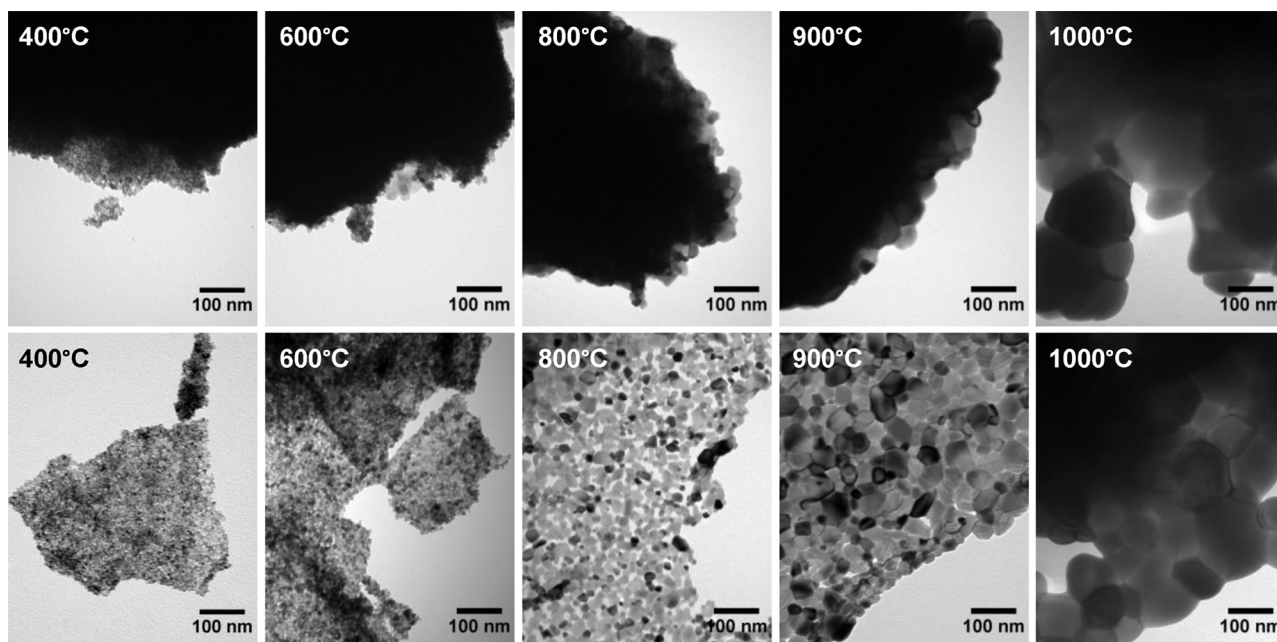


Fig. 2. (above) TEM micrographs of untemplated ceria particles, calcined in air between 400 and 1000 °C. (below) TEM micrographs of GO-templated ceria flakes, calcined in air between 400 and 1000 °C. Two-dimensional morphology is clearly retained for GO-templated ceria after thermal treatment.

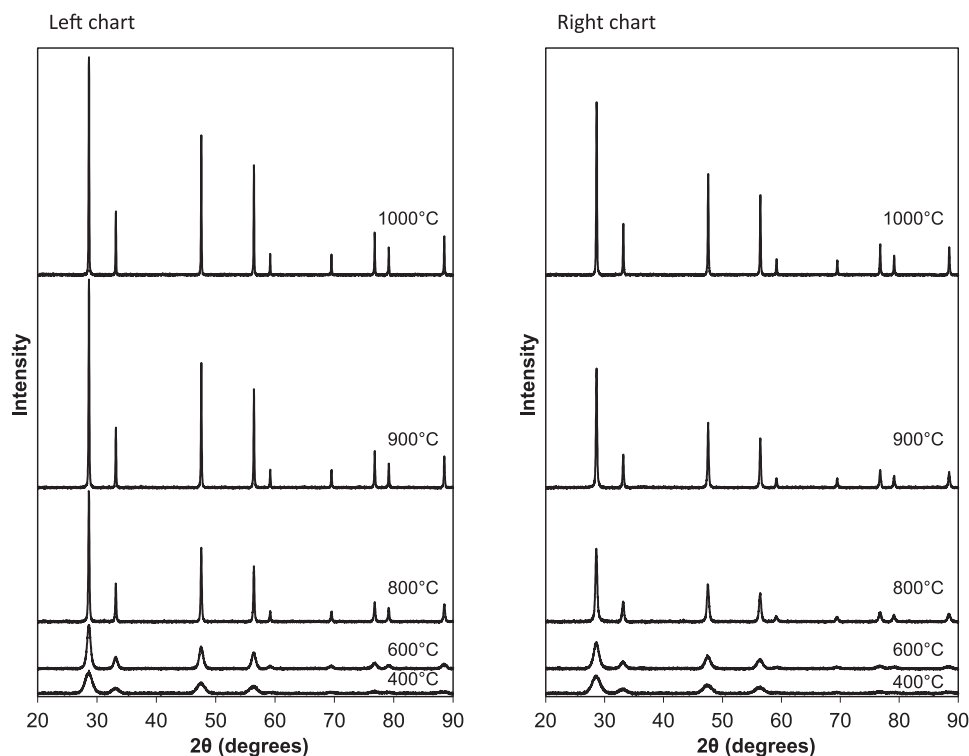


Fig. 3. Powder X-ray diffraction patterns for (left) untemplated ceria particles and (right) GO-templated ceria flakes, calcined between 400 and 1000 °C.

$-3.3(\Delta V/V_0)$ , where  $(\Delta a/a_0)$  is the change in the lattice constant. Therefore,  $\delta = 2.66(\Delta\omega/\omega_0)$  [49,50]. It should be noted that the peak shift in these samples is quite small ( $< 4 \text{ cm}^{-1}$ ), creating a degree of uncertainty. Furthermore, depending how far the Raman laser penetrates through the catalyst materials, this is a measure of oxygen vacancies at or near the surface of the particles. Nevertheless, the trend is clear – untemplated ceria particles show lower levels of oxygen vacancies than GO-templated ceria nanoflakes.

To further quantify oxygen vacancy levels in the ceria materials,

temperature-programmed reduction was performed, shown in Fig. 5. Typically, two TPR peaks are associated with nanostructured ceria - a lower-temperature peak associated to readily available surface oxygen reduction, and a higher-temperature peak representing the reduction of the bulk lattice oxygen [6,51]. As shown in Fig. 5a–b, both the GO-templated and untemplated ceria calcined at 400 and 600 °C clearly show both peaks. However, for the 800 °C calcination, this is greatly reduced for both samples. Table 2 shows the fraction of peaks intensities, clearly showing that the ceria flakes appear to retain more

**Table 1**  
Structural properties of ceria particles and GO-templated ceria nanoflakes.

Calcination T (°C)	Crystallite size (nm) <sup>a</sup>	BET surface area (m <sup>2</sup> /g)	Avg. pore diameter (cm <sup>3</sup> /g) <sup>b</sup>	Oxygen vacancies (%) <sup>c</sup>
Untemplated ceria particles				
400	5.9	116	33.9	2.7
600	10.7	18	33.3	1.3
800	35.4	1		0.8
900	48.7	< 1		0.9
1000	56.8	< 1		0.6
GO-templated ceria flakes				
400	5.4	113	29.1	3.3
600	7.1	43	38.8	3.2
800	21.4	9	49.8	1.4
900	30.5	6	41.5	0.9
1000	42.1	6	47.0	1.0

<sup>a</sup> Calculated using Scherrer equation using ceria (111) peak in XRD pattern.

<sup>b</sup> Calculated using Barret-Joyner-Halenda (BJH) method on desorption curves.

<sup>c</sup> Calculated from Raman spectra F2g band shift.

low-temperature surface reducibility than the untemplated ceria particles for all three calcination temperatures in agreement with the Raman spectra analysis.

The physical properties of both materials were also characterized by nitrogen adsorption. Both the GO-templated ceria flakes and untemplated ceria particles calcined at 400 °C show a type IV isotherm

(Fig. S2 in supporting information), characteristic of mesoporous materials [52]. The type H2 hysteresis loop displayed is characteristic of a non-uniform network of pores, in both size and shape [53]. In both cases, the type IV isotherm is maintained upon calcination at 600 °C. As shown in Fig. S2(a), nitrogen adsorption and desorption from untemplated ceria particles calcined at 800 °C and above is negligible. GO-templated ceria nanoflakes calcined at 400 °C show a pore size distribution with narrower pore diameters than untemplated ceria particles, shown in Fig. S3. However, upon calcination at 600 °C, both materials show a similar pore size distribution.

While both materials experience severe sintering at high temperatures, the GO-templated ceria nanoflakes maintain a higher BET surface area compared to untemplated ceria particles after calcination at the same temperature (Fig. 6 and Table 1). This improved thermal stability of the flake materials is in agreement with the crystallite sizes derived from powder XRD data.

The catalytic activity of GO-templated ceria flakes and untemplated ceria particles for CO oxidation is shown in Fig. 7. Catalysts were calcined in static air at 400, 600, or 800 °C respectively prior to testing. The GO-templated ceria flakes calcined at 400 °C achieves similar although slightly superior activity than the untemplated ceria particles up to 400 °C reaction conditions. At higher reaction temperatures (400–500 °C), considerably higher conversions are achieved with the ceria flakes compared to the particles due to their considerably lower in-situ sintering as shown by the smaller reduction on surface area above 400 °C (Table 1). At 500 °C, the ceria flakes achieve full conversion of CO to CO<sub>2</sub>, while the untemplated ceria particles only reach

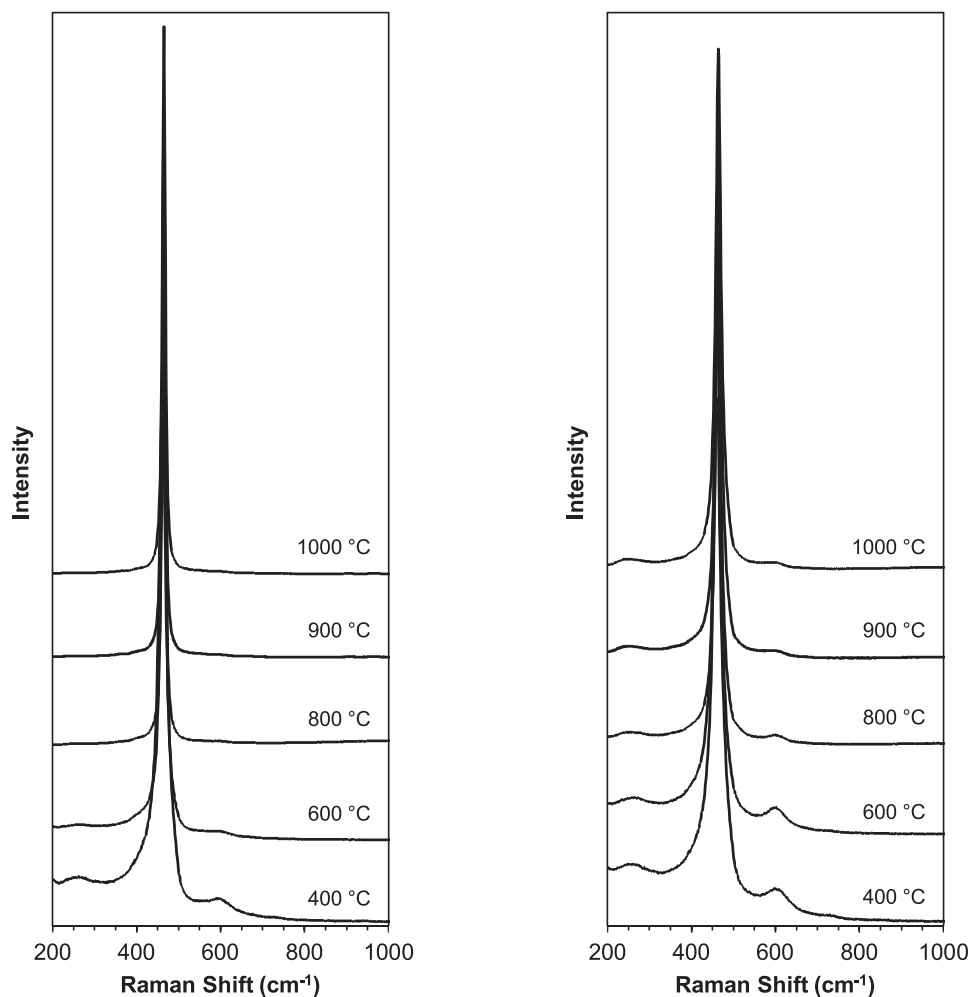


**Fig. 4.** Raman spectra of (left) untemplated ceria particles and (right) GO-templated ceria flakes, calcined between 400 and 1000 °C.

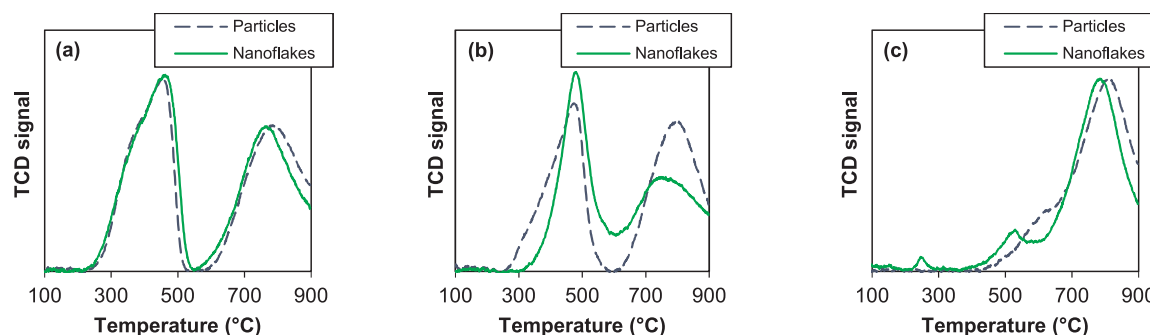


Fig. 5. TPR profiles for GO-templated ceria flakes and untemplated ceria particles calcined at (a) 400 °C, (b) 600 °C, and (c) 800 °C.

Table 2

Fraction of peak areas in TPR profiles for untemplated ceria particles and GO-templated ceria flakes.

Calcination T (°C)	Surface oxygen peak (fraction)	Bulk oxygen peak (fraction)
Untemplated ceria particles		
400	0.64	0.36
600	0.53	0.47
800	0.03	0.97
GO-templated ceria flakes		
400	0.71	0.29
600	0.65	0.35
800	0.06	0.94

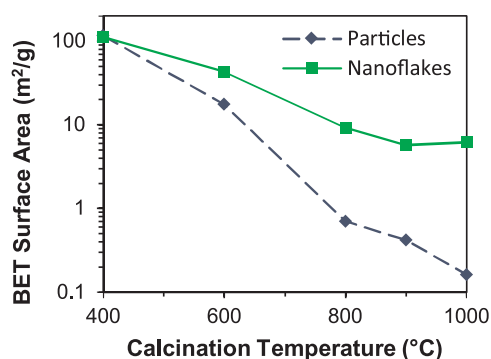


Fig. 6. (a) BET surface area vs. calcination temperature and for GO-templated ceria flakes and untemplated ceria particles.

approximately 80% conversion. GO-templated ceria flakes also outperformed the untemplated particles when calcined at 600 °C - at this calcination temperature the GO-templated ceria flakes are capable of maintaining a high surface area and high concentration of their initial surface oxygen concentration, critical for the CO oxidation reaction. In Fig. S4, this is shown in terms of turnover frequency (TOF) calculations at 450 °C. These results demonstrate that templating ceria with

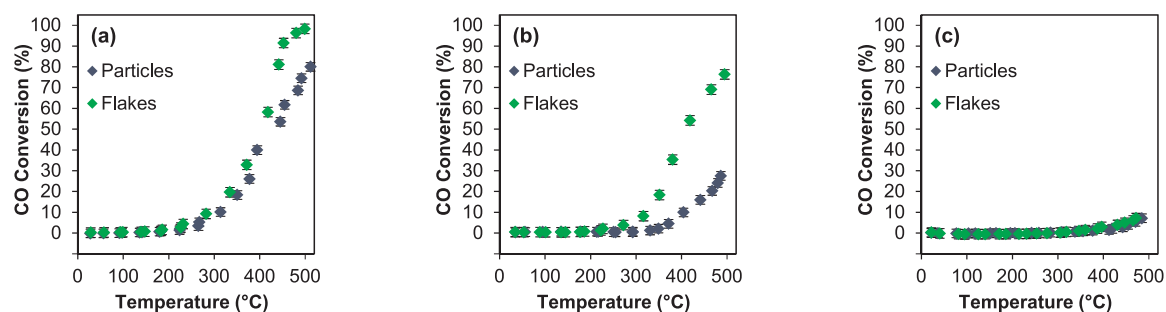


Fig. 7. Catalytic activity for CO oxidation of GO-templated ceria flakes and untemplated ceria particles, calcined at (a) 400 °C, (b) 600 °C, and (c) 800 °C.

sacrificial GO results in more thermally stable catalysts.

Templated ceria nanoflakes perform comparably to or slightly better than some nanostructured ceria catalysts recently reported in the literature for CO oxidation. At 250 °C, the turnover frequency of these ceria nanoflakes for CO oxidation (in terms of  $\mu\text{mol}$  of CO converted per g of catalyst) is  $19.1 \mu\text{mol g}^{-1} \text{min}^{-1}$ , while other papers show catalyst performance corresponding to  $14\text{--}20 \mu\text{mol g}^{-1} \text{min}^{-1}$  [54,55]. Other papers report catalysts with conversion rates corresponding to much higher TOF values; 53 and  $163 \mu\text{mol g}^{-1} \text{min}^{-1}$  for solvothermally prepared ‘cauliflower-like’ ceria and microwave-assisted hydrothermally synthesized ceria nanocubes, respectively [56,57]. However, it should be noted that variations in reaction conditions can limit comparability; in particular, significantly different  $\text{O}_2:\text{CO}$  ratios in reaction gas mixtures.

CO oxidation is a surface-catalyzed reaction, proceeding via the Mars-Van Krevelen mechanism [58]. Nevertheless, higher surface areas do not necessarily correlate with better catalytic performance, because, among other reasons, the nature of the exposed ceria crystal planes can influence activity [59]. In any case, prevention of excessive sintering is very important, as demonstrated with these ceria samples - where GO templating leads to smaller crystallite sizes and larger surface area upon calcination at 400–1000 °C, resulting in more active and thermally stable catalysts [6,60,61]. In addition, CO oxidation over ceria-based catalysts is rather sensitive to oxygen vacancy concentration in such a way that the greater the population of oxygen defects, the better the CO oxidation performance [62,63]. The observed catalytic trends correlate perfectly with the Raman and TPR experiments, which show how ceria nanoflakes retain a higher population of oxygen defects after thermal treatment compared to ceria nanoparticles and thus improved reducibility, exhibiting improved oxidation activity.

In addition to bare ceria nanoflakes and particles, nickel-loaded ceria nanoflakes and particles were synthesized as catalysts for the dry reforming of methane. Nickel is a common low-cost alternative to noble metal catalysts for this application. While noble metals such as Pt, Pd, or Rh typically retain higher stability, activity and resistance to coke formation than non-noble alternatives, the interaction between the metal and support can play a large role in modifying metal dispersion and electronic effects - and thus overall catalyst performance

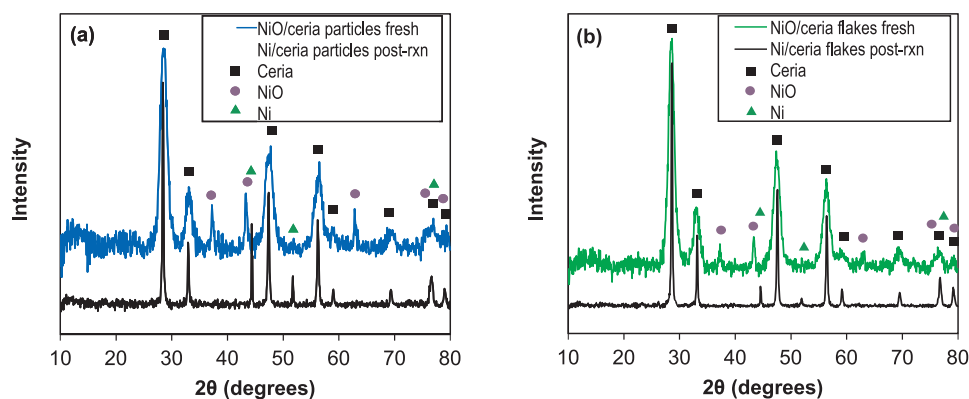


Fig. 8. Powder XRD patterns of Ni-ceria catalysts, pre- and post-reaction. (a) Untemplated Ni-ceria particles. (b) GO-templated Ni-ceria flakes.

[26,64–66]. Here, the effect of using GO-templated ceria nanoflakes vs. untemplated ceria particles as a support for nickel is explored.

Powder XRD patterns of the Ni-ceria samples are shown in Fig. 8. After nickel deposition and calcination at 700 °C, but pre-reaction, NiO is visible in the diffraction pattern. Using the Scherrer equation, the sizes of the ceria crystallites are calculated to be 6.6 and 5.7 nm on templated ceria flakes and untemplated ceria particles, respectively, while the size of NiO particles is calculated to be 20 and 24 nm, respectively. These values are broadly similar, given the limitations of Scherrer equation calculations, indicating that both templated Ni-ceria flakes and untemplated Ni-ceria particles initially have similar crystallite sizes for both the ceria and NiO components of the catalyst.

Additionally, TPR experiments were conducted on the Ni-deposited ceria nanoflakes and particles, shown in Fig. 9. The TPR profiles are similar to the ones of the bare ceria materials (Fig. 5) with the addition of low temperature peaks (< 400 °C), attributable to NiO reduction. The lowest temperature (~200 °C) peak can be attributed to the reduction of larger “free” NiO not bound to the ceria support, while the higher-temperature peak (at ~325 °C) is attributed to NiO bound to the surface of ceria [67,68]. For this main peak, the NiO-ceria nanoflake TPR profile shows a shift to higher reduction temperatures compared with the NiO-ceria particle sample. There are two possible explanations for this. The size of NiO particles can affect the reduction temperature, so this is possibly indicative of different NiO particle sizes on the ceria nanoflake sample [69,70]. Alternatively, metal-support interactions can influence the reduction temperature as well. In the case of nickel-ceria, stronger interaction between NiO and the ceria support results in higher reduction temperatures [71,72]. XRD analysis showed that the NiO crystallite sizes in the nanoflake and untemplated particle systems were similar, so the shift to a higher reduction temperature is likely due to differences in NiO-ceria interaction in the two catalysts. A shoulder extending from approximately 450 to 500 °C is visible for the NiO/ceria

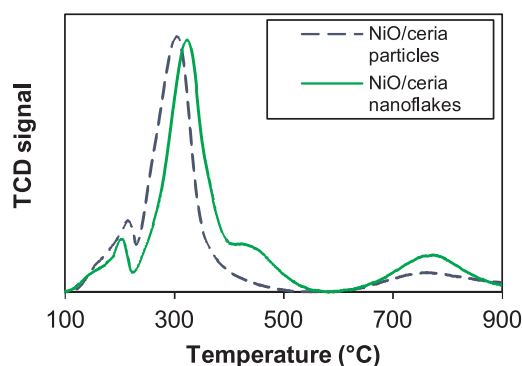


Fig. 9. TPR profiles for nickel-deposited GO-templated ceria flakes and untemplated ceria particles.

nanoflake TPR profile, but not the NiO/ceria particle sample, attributed to readily available surface oxygen in the ceria flakes.

TEM micrographs of the fresh Ni-loaded ceria flakes and particles are shown in Fig. 10a–b. EDX analyses and maps (Figs. S6–8) show that the smaller (< 10 nm) crystallites are primarily ceria, while the larger (20–40 nm) crystallites are nickel (NiO according to XRD). These ceria crystallite sizes match those calculated using Scherrer equation analysis using the ceria XRD patterns in Fig. 3 (~6 nm for both materials, Table 1), and Ni-loaded ceria XRD patterns in Fig. 8. In Fig. 10a, of the fresh Ni-loaded ceria flakes, NiO particles can be seen clustering around the edges of ceria crystallite agglomerations. However, for the fresh untemplated Ni-loaded ceria particles, shown in Fig. 10b, while some NiO particles appear to be similarly deposited on the edge of ceria crystallite agglomerations, much of the visible nickel is not deposited on ceria. These un-supported NiO particles were evenly dispersed across the TEM sample grid, a phenomenon not observed with the Ni-ceria flake sample. This observation suggests that NiO particles have a better interaction with the ceria support when supported on ceria flakes than ceria particles in agreement with the TPR data. Surface defects such as oxygen vacancies are known to be preferential nucleation sites for metal particle formation [73,74]. Therefore, the ceria flakes promote better nickel dispersion and stronger Ni-ceria interaction than the ceria particles, in agreement with the higher surface oxygen vacancy concentration of the nanoflakes, seen in Raman and TPR analysis.

Catalytic activity of the Ni-loaded ceria particles and flakes for the dry reforming of methane (DRM) is shown in Fig. 11a–b. In both cases, conversion of CH<sub>4</sub> is lower than conversion of CO<sub>2</sub> across the temperature range tested, a common observation in DRM because methane activation is the rate-limiting step [75]. For CO<sub>2</sub>, conversion levels range from approximately 20% at 550 °C to 90% at 850 °C, while CH<sub>4</sub> conversion levels are less than 5% and 60–65% at 550 and 850 °C, respectively. The ratio of H<sub>2</sub> to CO produced ranges from 0.5 to 0.8 across the same temperature range. While this is promising, conversion levels do not appear to be as high as other nickel-based DRM catalysts recently reported in the literature. However, with papers reporting wide variation in Ni loading (1 to 63.5%), reduction temperatures, space velocity and gas ratios, results are not always directly comparable [76]. The Ni supported on ceria flakes and particles perform similarly, although there are small differences. In both cases, the syngas H<sub>2</sub>/CO ratio is close to 1 at high reaction temperatures, which is the limit imposed by the stoichiometry of the reaction.

Longer-term studies of the dry reforming reaction were undertaken at 800 °C, shown in Fig. 11c–d. In contrast with the short-term temperature curve experiment shown in Fig. 11a, where there were only small differences, in a long-term experiment the difference in activity between the two catalysts is quite dramatic. Untemplated Ni-ceria particles experience severe deactivation after approximately 5 h, while the Ni-ceria flakes demonstrated much higher stability for both CH<sub>4</sub>/CO<sub>2</sub> conversion and maintaining a high H<sub>2</sub>/CO ratio. This can also be

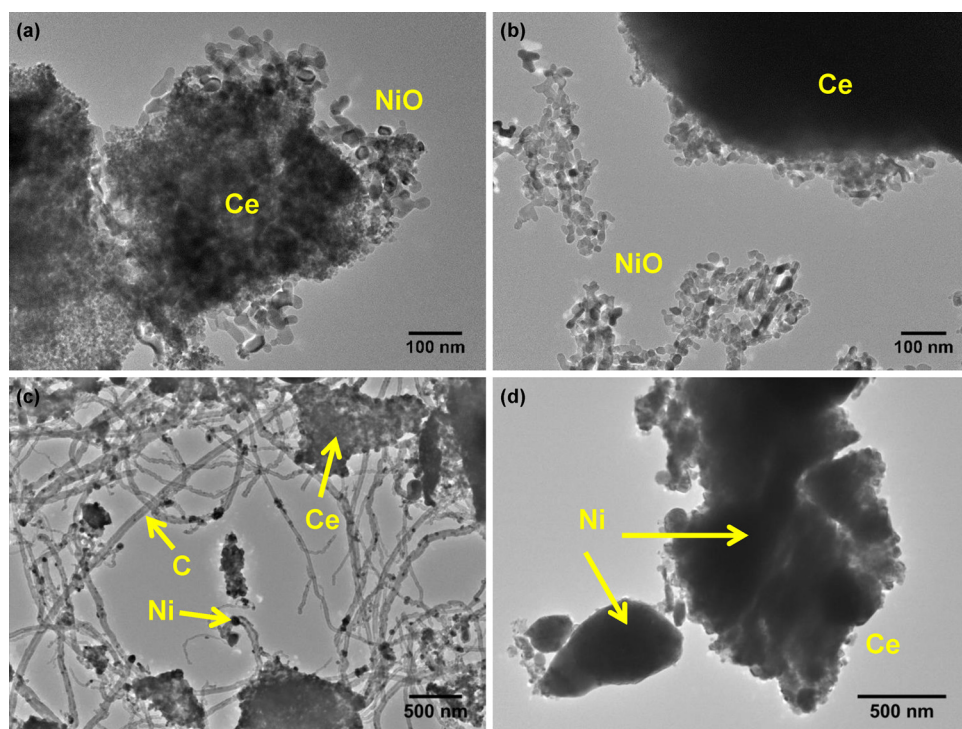


**Fig. 10.** TEM micrographs of Ni-ceria catalysts, both fresh and post-methane reforming reaction. Dark and light areas are Ni and ceria, respectively. (a) Fresh Ni-ceria flake catalyst after calcination at 700 °C. (b) Fresh Ni-ceria particle catalyst after calcination at 700 °C. (c) Post-20 h, 800 °C reaction Ni-ceria flake catalyst. (d) Post 20 h, 800 °C reaction Ni-ceria particle catalyst.

seen in the TOF values (Fig. S5) – for both CH<sub>4</sub> and CO<sub>2</sub> conversion over the 20-hour reaction, the activity of the Ni-ceria particles decreases significantly more than the activity of the Ni-ceria flakes. After 20 h, the Ni-ceria flakes experience a reduction in activity of 18% for CO<sub>2</sub> conversion and 40% for CH<sub>4</sub> conversion, while the activity of Ni-ceria

particles is reduced by 66% and 89%, respectively. Although only small improvements in activity are initially achieved with the ceria flakes compared with ceria particles, the main benefit of utilizing GO-templated ceria flakes is the improved thermal stability and resistance to sintering that is due to the stronger nickel-ceria interaction of the ceria

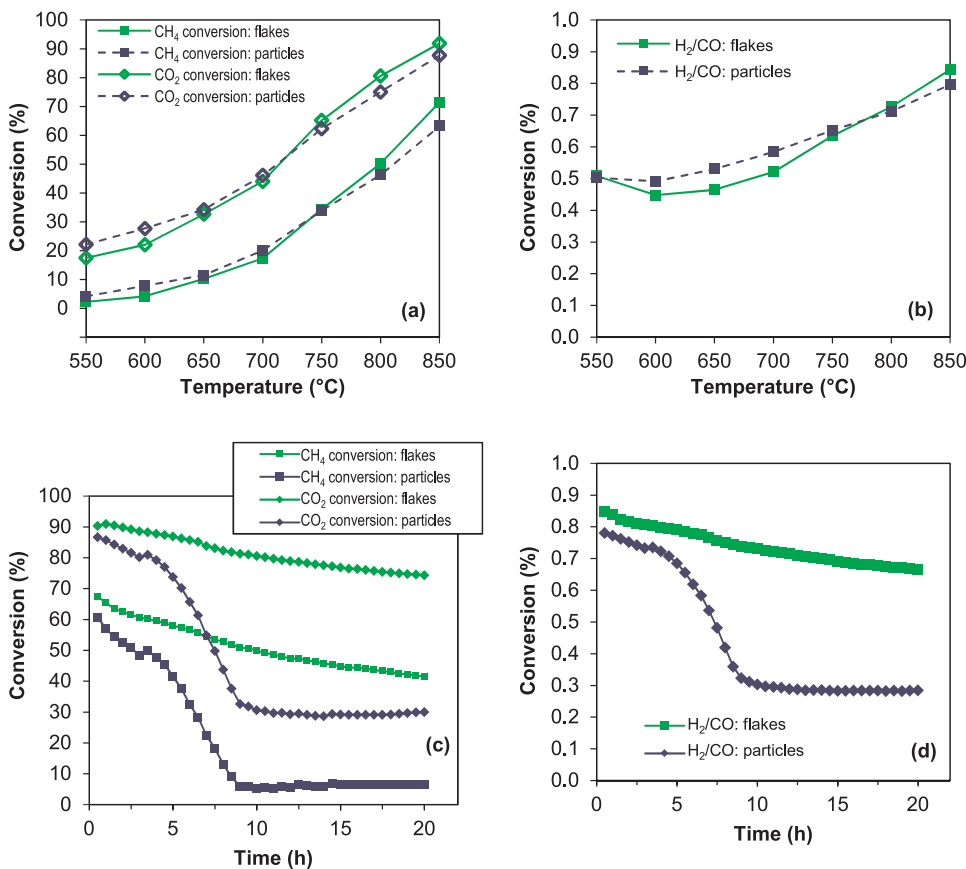


**Fig. 11.** (a) Catalytic activity of Ni-loaded ceria flakes and particles for the dry reforming of methane, showing both CH<sub>4</sub> and CO<sub>2</sub> conversion. (b) The ratio of H<sub>2</sub> to CO produced as a function of temperature. (c) Long-term catalytic activity of Ni-loaded ceria flakes and particles at 800 °C for the dry reforming of methane, showing both CH<sub>4</sub> and CO<sub>2</sub> conversion. (d) The ratio of H<sub>2</sub> to CO produced as a function of time at 800 °C.

flakes.

Nickel sintering and carbon deposition are the two major causes of catalyst deactivation of Ni based catalysts for dry methane reforming [77]. Post-reaction analysis was undertaken to determine the significance of these factors. Post-reaction powder XRD patterns are shown in Fig. 8. Compared with the pre-reaction patterns, nickel is now present as Ni instead of NiO. Similarly to the pre-reaction NiO-ceria samples, the ceria crystallite sizes are similar in the spent catalysts – 34.4 and 33.1 nm for flakes and particles, respectively. In contrast, the Ni metal particles deposited on the post-reaction ceria particles are calculated to be 56 nm, compared with 43 nm for post-reaction ceria nanoflakes. This is an indication that while ceria nanoflakes do not entirely prevent nickel sintering, they do hinder sintering in comparison to nickel particles deposited on untemplated ceria, and shows that the Ni particles are better dispersed on ceria flakes than ceria particles post-reaction, in agreement with the TPR results.

TEM micrographs of post-reaction spent Ni-ceria catalysts are shown in Fig. 10c–d. After the 20 h stability experiment, the Ni-ceria flake catalyst, shown in Fig. 10c, has retained its two-dimensional structure. However, the nickel particles have sintered, showing a wide range of sizes. Additionally, the ceria flakes are surrounded by a network of carbon nanotubes. In comparison, the Ni-loaded ceria particle catalyst is shown in Fig. 10d. While the large ceria agglomerations seen in Fig. 10b are still evident, the nickel is now also present in very large agglomerations being difficult to distinguish any structure at the nanoscale. Furthermore, no carbon nanotubes are visible. While both the Ni-ceria flake and Ni-ceria particle catalysts show sintering of the nickel particles (Figs. 10c–d, S9–11), the sintering appears to be more severe for the untemplated Ni-ceria particle catalyst. The nanoflake catalyst shows a wide range of Ni particle sizes, from < 100 nm to ~500 nm, while the untemplated particle catalyst only shows 300–500 nm and larger Ni particles.

TGA was performed on the post-20 h reaction Ni-ceria catalysts, shown in Fig. 12. The TGA curve of the Ni-ceria flakes shows a sharp decrease in mass at approximately 500–600 °C, indicative of the presence of deposited carbon on the catalyst after reaction. However, the Ni-ceria particles do not show a similar decrease in mass. This indicates that significant carbon deposition occurred on the Ni-ceria flakes, but not the Ni-ceria particles, confirming a different reaction behavior, and correlates well with TEM post-reaction analysis.

In summary, the post-reaction analysis indicates that nickel sintering, and not carbon deposition, is responsible for the significant difference in catalyst deactivation in the long-term DRM experiment between the GO-templated and untemplated Ni-ceria catalysts. While both catalysts experienced nickel sintering, the untemplated Ni-ceria particle catalyst suffered from more severe sintering (Fig. 10c–d, S6). While TGA analysis (Fig. 12) showed carbon formation for the Ni-ceria flake catalyst and not the Ni-ceria particle catalyst, the TEM images

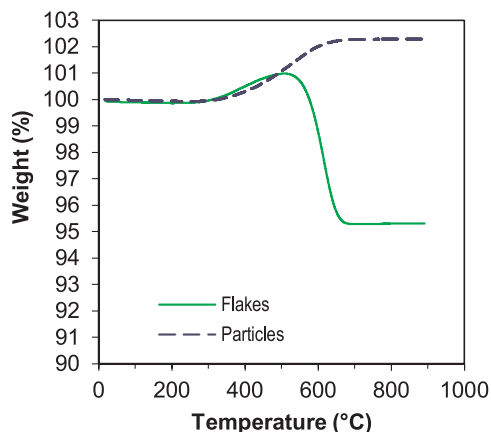


Fig. 12. TGA curves for post-20 h reaction Ni-ceria flakes and particles in air.

(Fig. 10c) showed that this was a network of filamentous carbon. Carbon deposition has often been reported to be a significant factor in nickel catalyst deactivation [78–80]. However, the type of carbon deposit - encapsulating, filamentous, or other - affects methane reforming catalysts in different ways, if at all, and the relationship between catalytic activity and quantity of carbon deposited on the catalyst is not always straightforward [81]. While the formation of amorphous carbon can coat and deactivate catalysts, filamentous carbon growth can lead to structural modifications within the catalyst (such as forced separation of the nickel and ceria crystallites) which reduces activity [82]. Nevertheless, not all filamentous carbon growth appears to be harmful to catalytic activity. Additionally, it should be underlined that carbon formation is difficult to avoid for Ni-based materials during methane reforming reaction and the formation of carbon (soft or hard) is an indication of catalytic activity [63]. The key is developing Ni-based materials which lead to soft carbon formation, which is possible if Ni sintering is hindered, since large Ni clusters are more prone to forming hard carbon deposits than small Ni clusters [64,83]. In this scenario, Ni-ceria nanoflakes are excellent materials due to their resistance towards metallic sintering.

Overall, GO-templated ceria flakes outperform untemplated ceria particles for both CO oxidation and, with nickel deposition, the dry reforming of methane. Their improved resistance to sintering, higher BET surface area after exposure to high temperatures, and higher surface reducibility leads to a clear stability advantage in high-temperature reactions.

#### 4. Conclusions

In conclusion, sintering-resistant GO-templated ceria nanoflakes have been successfully synthesized via a room-temperature precipitation reaction. The improved textural properties provided by GO templating result in a ceria catalyst capable of maintaining a higher surface area than untemplated ceria particles when calcined above 400 °C, demonstrating lower crystallite growth and improved resistance to sintering. Furthermore, Raman and TPR analysis show that GO-templated ceria flakes have a higher level of oxygen vacancies than untemplated ceria particles. For these reasons, GO-templated ceria flakes demonstrate improved catalytic activity for CO oxidation. Ceria flakes also inhibit sintering of deposited nickel particles when compared with nickel deposited on untemplated ceria particles. This presents advantages for the dry reformation of methane, where Ni/GO-templated ceria flakes maintains a considerably higher activity for the conversion of both methane and carbon dioxide than untemplated Ni/ceria particles in long-term stability tests.

It should be noted that, while more sintering-resistant than untemplated ceria particles, the nanoflakes do still lose specific surface area with exposure to high temperatures. Future research will include steps to mitigate this behavior further – for example, by investigating the applicability of GO templating to ceria-zirconia mixed oxides or the inclusion of other promoters such as Nd, Pr, La, etc. which are known to improve thermal stability in applications such as automotive catalysis.

The capability to produce thermally stable ceria-based materials which limit high-temperature sintering is critical for ceria's further development across a range of environmentally applications. The use of GO as a sacrificial template offers a potential route for synthesizing thermally stable ceria catalysts, one in which a simple precipitation reaction is utilized and the template easily removed post-synthesis.

#### Acknowledgements

This work was supported by the Engineering and Physical Sciences Research Council (EPSRC) [grant numbers EP/L016354/1, EP/R512904/1, EP/P008097/1, and EP/L020432/2]. The authors would like to thank the Microscopy and Analysis Suite (MAS) at the University of Bath for assistance with TEM and Raman characterization.

Experimental data is available via the University of Bath Research Data Archive (DOI: <https://doi.org/10.15125/BATH-00514>).

## Appendix A. Supplementary data

Supplementary material related to this article can be found, in the online version, at doi:<https://doi.org/10.1016/j.apcatb.2018.10.011>.

## References

- [1] T. Montini, M. Melchionna, M. Monai, P. Fornasiero, Fundamentals and catalytic applications of CeO<sub>2</sub>-based materials, *Chem. Rev.* 116 (2016) 5987–6041, <https://doi.org/10.1021/acs.chemrev.5b00603>.
- [2] Z.P. Shao, S.M. Haile, A high-performance cathode for the next generation of solid-oxide fuel cells, *Nature* 431 (2004) 170–173, <https://doi.org/10.1038/nature02863>.
- [3] B. Zhang, X. Tang, Y. Li, Y. Xu, W. Shen, Hydrogen production from steam reforming of ethanol and glycerol over ceria-supported metal catalysts, *Int. J. Hydrogen Energy* 32 (2007) 2367–2373, <https://doi.org/10.1016/j.ijhydene.2006.11.003>.
- [4] G.R. Bamwenda, H. Arakawa, Cerium dioxide as a photocatalyst for water decomposition to O<sub>2</sub> in the presence of Ce(aq)(4+) and Fe(aq)(3+) species, *J. Mol. Catal. A: Chem.* 161 (2000) 105–113, [https://doi.org/10.1016/S1381-1169\(00\)00270-3](https://doi.org/10.1016/S1381-1169(00)00270-3).
- [5] F. Lin, M. Rothensteiner, I. Alkneit, J.A. van Bokhoven, A. Wokaun, First demonstration of direct hydrocarbon fuel production from water and carbon dioxide by solar-driven thermochemical cycles using rhodium–ceria, *Energy Environ. Sci.* 9 (2016) 2400–2409, <https://doi.org/10.1039/C6EE00862C>.
- [6] L. Torrente-Murciano, A. Gilbank, B. Puertollas, T. Garcia, B. Solsona, D. Chadwick, Shape-dependency activity of nanostructured CeO<sub>2</sub> in the total oxidation of polycyclic aromatic hydrocarbons, *Appl. Catal. B-Environ.* 132–133 (2013) 116–122, <https://doi.org/10.1016/j.apcatb.2012.10.030>.
- [7] J.M. López, A.L. Gilbank, T. García, B. Solsona, S. Agouram, L. Torrente-Murciano, The prevalence of surface oxygen vacancies over the mobility of bulk oxygen in nanostructured ceria for the total toluene oxidation, *Appl. Catal. B-Environ.* 174 (2015) 403–412, <https://doi.org/10.1016/j.apcatb.2015.03.017>.
- [8] L. Torrente-Murciano, F.R. Garcia-Garcia, Effect of nanostructured support on the WGS activity of Pt/CeO<sub>2</sub> catalysts, *Catal. Commun.* 71 (2015) 1–6, <https://doi.org/10.1016/j.catcom.2015.07.021>.
- [9] M.V. Twigg, Catalytic control of emissions from cars, *Catal. Today* 163 (2011) 33–41, <https://doi.org/10.1016/j.cattod.2010.12.044>.
- [10] M.-S. Fan, A.Z. Abdullah, S. Bhatia, Catalytic technology for carbon dioxide reforming of methane to synthesis gas, *ChemCatChem* 1 (2009) 192–208, <https://doi.org/10.1002/cctc.200900025>.
- [11] X. Du, D. Zhang, L. Shi, R. Gao, J. Zhang, Morphology dependence of catalytic properties of Ni/CeO<sub>2</sub> nanostructures for carbon dioxide reforming of methane, *J. Phys. Chem. C* 116 (2012) 10009–10016, <https://doi.org/10.1021/jp300543r>.
- [12] C. Tang, L. Liping, L. Zhang, L. Tan, L. Dong, High carbon-resistance Ni@CeO<sub>2</sub> core-shell catalysts for dry reforming of methane, *Kinet. Catal.* 58 (2017) 800–808, <https://doi.org/10.1134/S0023158418010123>.
- [13] X. Zhao, M. Lu, H. Li, J. Fang, L. Shi, D. Zhang, In situ preparation of Ni nanoparticles in cerium-modified silica aerogels for coking- and sintering-resistant dry reforming of methane, *New J. Chem.* 41 (2017) 4869–4878, <https://doi.org/10.1039/C7NJ00115K>.
- [14] S. Abanades, G. Flamant, Thermochemical hydrogen production from a two-step solar-driven water-splitting cycle based on cerium oxides, *Sol. Energy* 80 (2006) 1611–1623, <https://doi.org/10.1016/j.solener.2005.12.005>.
- [15] S. Akbayrak, Y. Tonbul, S. Özkur, Nanoceria supported palladium(0) nanoparticles: super catalyst in dehydrogenation of formic acid at room temperature, *Appl. Catal. B: Environ.* 206 (2017) 384–392, <https://doi.org/10.1016/j.apcatb.2017.01.063>.
- [16] L. Torrente-Murciano, R.S.L. Chapman, A. Narvaez-Dinamarca, D. Mattia, M.D. Jones, Effect of nanostructured ceria as support for the iron catalysed hydrogenation of CO<sub>2</sub> into hydrocarbons, *Phys. Chem. Chem. Phys.* 18 (2016) 15496–15500, <https://doi.org/10.1039/C5CP07788E>.
- [17] J.L. Gasser-Ramirez, B.C. Dunn, D.W. Ramirez, E.P. Fillerup, G.C. Turpin, Y. Shi, R.D. Ernst, R.J. Pugmire, E.M. Eyring, K.A. Pettigrew, A simple synthesis of catalytically active, high surface area ceria aerogels, *J. Non-Cryst. Solids* 354 (2008) 5509–5514, <https://doi.org/10.1016/j.jnoncrsol.2008.09.011>.
- [18] S. Kurajica, I. Minga, M. Guliš, V. Mandić, I. Simčić, High surface area ceria nanoparticles via hydrothermal synthesis experiment design, *J. Nanomater.* 2016 (2016), <https://doi.org/10.1155/2016/7274949>.
- [19] J. Yang, L. Lukashuk, H. Li, K. Föttinger, G. Rupprechter, U. Schubert, High surface area ceria for CO oxidation prepared from cerium t-butoxide by combined sol-gel and solvothermal processing, *Catal. Lett.* 144 (2014) 403–412, <https://doi.org/10.1007/s10562-013-1162-8>.
- [20] D. Zhang, X. Du, L. Shi, R. Gao, Shape-controlled synthesis and catalytic application of ceria nanomaterials, *Dalton Trans.* 41 (2012) 14455–14475, <https://doi.org/10.1039/C2DT31759A>.
- [21] J. Han, J. Meeprasert, P. Maitarad, S. Nammuangruk, L. Shi, D. Zhang, Investigation of the facet-dependent catalytic performance of Fe<sub>2</sub>O<sub>3</sub>/CeO<sub>2</sub> for the selective catalytic reduction of NO with NH<sub>3</sub>, *J. Phys. Chem. C* 120 (2016) 1523–1533, <https://doi.org/10.1021/acs.jpcc.5b09834>.
- [22] P. Maitarad, J. Han, D. Zhang, L. Shi, S. Nammuangruk, T. Rungrotmongkol, Structure–activity relationships of NiO on CeO<sub>2</sub> nanorods for the selective catalytic reduction of NO with NH<sub>3</sub>: experimental and DFT studies, *J. Phys. Chem. C* 118 (2014) 9612–9620, <https://doi.org/10.1021/jp5024845>.
- [23] Z. Gao, L.V. Mogni, E.C. Miller, J.G. Railsback, S.A. Barnett, A perspective on low-temperature solid oxide fuel cells, *Energy Environ. Sci.* 9 (2016) 1602–1644, <https://doi.org/10.1039/C5EE03858H>.
- [24] J.-J. He, C.-X. Wang, T.-T. Zheng, Y.-K. Zhao, Thermally induced deactivation and the corresponding strategies for improving durability in automotive three-way catalysts, *Johnson Matthey Tech.* 60 (2016) 196–203, <https://doi.org/10.1595/205651316x691960>.
- [25] J.R. Scheffe, A. Steinfeld, Oxygen exchange materials for solar thermochemical splitting of H<sub>2</sub>O and CO<sub>2</sub>: a review, *Mater. Today* 17 (2014) 341–348, <https://doi.org/10.1016/j.mattod.2014.04.025>.
- [26] D. Pakhare, J. Spivey, A review of dry (CO<sub>2</sub>) reforming of methane over noble metal catalysts, *Chem. Soc. Rev.* 43 (2014) 7813–7837, <https://doi.org/10.1039/C3CS60395D>.
- [27] T.K. Kim, K.J. Lee, J.Y. Cheon, J.H. Lee, S.H. Joo, H.R. Moon, Nanoporous metal oxides with tunable and nanocrystalline frameworks via conversion of metal-organic frameworks, *J. Am. Chem. Soc.* 135 (2013) 8940–8946, <https://doi.org/10.1021/ja401869h>.
- [28] S. Wang, J. Zhang, J. Jiang, R. Liu, B. Zhu, M. Xu, Y. Wang, J. Cao, M. Li, Z. Yuan, S. Zhang, W. Huang, S. Wu, Porous ceria hollow microspheres: synthesis and characterization, *Microporous Mesoporous Mater.* 123 (2009) 349–353, <https://doi.org/10.1016/j.micromeso.2009.04.020>.
- [29] D. Zhang, C. Pan, L. Shi, L. Huang, J. Fang, H. Fu, A highly reactive catalyst for CO oxidation: CeO<sub>2</sub> nanotubes synthesized using carbon nanotubes as removable templates, *Microporous Mesoporous Mater.* 117 (2009) 193–200, <https://doi.org/10.1016/j.micromeso.2008.06.022>.
- [30] G. Hua, L. Zhang, G. Fei, M. Fang, Enhanced catalytic activity induced by defects in mesoporous ceria nanotubes, *J. Mater. Chem.* 22 (2012) 6851–6855, <https://doi.org/10.1039/C2JM13610D>.
- [31] G. Mondragón-Galicia, R. Pérez-Hernández, C.E. Gutiérrez-Wing, D. Mendoza-Anaya, A novel synthesis method to produce silver-doped CeO<sub>2</sub> nanotubes based on Ag nanowire templates, *Phys. Chem. Chem. Phys.* 13 (2011) 16756–16761, <https://doi.org/10.1039/c1cp21017c>.
- [32] Y. Chen, J. Lu, Facile fabrication of porous hollow CeO<sub>2</sub> microspheres using polystyrene spheres as templates, *J. Porous Mater.* 19 (2012) 289–294, <https://doi.org/10.1007/s10934-011-9474-9>.
- [33] N.C. Strandwitz, G.D. Stucky, Hollow microporous cerium oxide spheres templated by colloidal silica, *Chem. Mater.* 21 (2009) 4577–4582, <https://doi.org/10.1021/cm901516b>.
- [34] S. Eslava, A. Reynal, V.G. Rocha, S. Barg, E. Saiz, Using graphene oxide as a sacrificial support of polyoxotitanium clusters to replicate its two-dimensionality in pure titania photocatalysts, *J. Mater. Chem. A* 4 (2016) 7200–7206, <https://doi.org/10.1039/C5TA09989G>.
- [35] D.R. Dreyer, A.D. Todd, C.W. Bielawski, Harnessing the chemistry of graphene oxide, *Chem. Soc. Rev.* 43 (2014) 5288–5301, <https://doi.org/10.1039/c4cs00060a>.
- [36] G. Zhao, J. Li, L. Jiang, H. Dong, X. Wang, W. Hu, Synthesizing MnO<sub>2</sub> nanosheets from graphene oxide templates for high performance pseudosupercapacitors, *Chem. Sci.* 3 (2012) 433–437, <https://doi.org/10.1039/C1SC00722J>.
- [37] D.C. Marcano, D.V. Kosynkin, J.M. Berlin, A. Sinitskii, Z. Sun, A. Slesarev, L.B. Alemany, W. Lu, J.M. Tour, Improved synthesis of graphene oxide, *ACS Nano* 4 (2010) 4806–4814, <https://doi.org/10.1021/nn1006368>.
- [38] G. Zhang, Y. Guo, L. Lu, Z. Zhang, L. Wang, L. Zhou, J. Shao, Synthesis and characterization of CeO<sub>2</sub> thin film with well-ordered step edges, *Mater. Lett.* 125 (2014) 162–166, <https://doi.org/10.1016/j.matlet.2014.03.157>.
- [39] L. Jiang, M. Yao, B. Liu, Q. Li, R. Liu, H. Lv, S. Lu, C. Gong, B. Zou, T. Cui, Controlled synthesis of CeO<sub>2</sub>/graphene nanocomposites with highly enhanced optical and catalytic properties, *J. Phys. Chem. C* 116 (2012) 11741–11745, <https://doi.org/10.1021/jp3015113>.
- [40] K. Huang, Y.H. Li, S. Lin, C. Liang, X. Xu, Y.F. Zhou, D.Y. Fan, H.J. Yang, P.L. Lang, R. Zhang, One-step synthesis of reduced graphene oxide–CeO<sub>2</sub> nanocubes composites with enhanced photocatalytic activity, *Mater. Lett.* 124 (2014) 223–226, <https://doi.org/10.1016/j.matlet.2014.03.023>.
- [41] T.S. Sakhitvel, S. Das, C.J. Pratt, S. Seal, One-pot synthesis of a ceria–graphene oxide composite for the efficient removal of arsenic species, *Nanoscale* 9 (2017) 3367–3374, <https://doi.org/10.1039/C6NR07608D>.
- [42] M. Guo, J. Lu, Y. Wu, Y. Wang, M. Luo, UV and visible Raman studies of oxygen vacancies in rare-earth-doped ceria, *Langmuir* 27 (2011) 3872–3877, <https://doi.org/10.1021/la200292f>.
- [43] Y. She, Q. Zheng, L. Li, Y. Zhan, C. Chen, Y. Zheng, X. Lin, Rare earth oxide modified CuO/CeO<sub>2</sub> catalysts for the water–gas shift reaction, *Int. J. Hydrogen Energy* 34 (2009) 8929–8936, <https://doi.org/10.1016/j.ijhydene.2009.08.062>.
- [44] S.A. Acharya, V.M. Gaikwad, V. Sathe, S.K. Kulkarni, Influence of gadolinium doping on the structure and defects of ceria under fuel cell operating temperature, *Appl. Phys. Lett.* 104 (2014) 113508, <https://doi.org/10.1063/1.4869116>.
- [45] J.R. McBride, K.C. Hass, B.D. Poindexter, W.H. Weber, Raman and x-ray studies of Ce<sub>1-x</sub>RExO<sub>2-y</sub>, where RE = La, Pr, Nd, Eu, Gd, and Tb, *J. Appl. Phys.* 76 (1994) 2435, <https://doi.org/10.1063/1.357593>.
- [46] T. Taniguchi, T. Watanabe, N. Sugiyama, A.K. Subramani, H. Wagata, N. Matsushita, M. Yoshimura, Identifying defects in ceria-based nanocrystals by UV resonance Raman spectroscopy, *J. Phys. Chem. C* 113 (2009) 19789–19793, <https://doi.org/10.1021/jp9049457>.
- [47] A. Younis, D. Chu, Y.V. Kaneti, S. Li, Tuning the surface oxygen concentration of {111} surrounded ceria nanocrystals for enhanced photocatalytic activities,

- Nanoscale 8 (2016) 378–387, <https://doi.org/10.1039/C5NR06588G>.
- [48] Yuan-Pei Lan, Hong Sohn, Yong, Effect of oxygen vacancies and phases on catalytic properties of hydrogen-treated nanoceria particles, *Mater. Res. Express.* 5 (2018) 035501, <https://doi.org/10.1088/2053-1591/aaaff4>.
- [49] Y. Lee, G. He, A.J. Akey, R. Si, M. Flytzani-Stephanopoulos, I.P. Herman, Raman analysis of mode softening in nanoparticle CeO<sub>2</sub>– $\delta$  and Au-CeO<sub>2</sub>– $\delta$  during CO oxidation, *J. Am. Chem. Soc.* 133 (2011) 12952–12955, <https://doi.org/10.1021/ja204479j>.
- [50] S.R. Bishop, K.L. Duncan, E.D. Wachsman, Defect equilibria and chemical expansion in non-stoichiometric undoped and gadolinium-doped cerium oxide, *Electrochim. Acta* 54 (2009) 1436–1443, <https://doi.org/10.1016/j.electacta.2008.09.026>.
- [51] H. Sohn, G. Celik, S. Gunduz, D. Dogu, S. Zhang, J. Shan, F.F. Tao, U.S. Ozkan, Oxygen mobility in pre-reduced nano- and macro-ceria with co loading: an AP-XPS, in-situ DRIFTS and TPR study, *Catal. Lett.* 147 (2017) 2863–2876, <https://doi.org/10.1007/s10562-017-2176-4>.
- [52] K.S.W. Sing, D.H. Everett, R.A.W. Haul, L. Moscou, R.A. Pierotti, J. Rouquerol, T. Siemieniowska, Reporting physisorption data for gas/solid systems with special reference to the determination of surface area and porosity, *Pure Appl. Chem.* 54 (1982) 2201–2218, <https://doi.org/10.1515/iupac.57.0007>.
- [53] G. Leofanti, M. Padovan, G. Tozzola, B. Venturelli, Surface area and pore texture of catalysts, *Catal. Today* 41 (1998) 207–219, [https://doi.org/10.1016/S0920-5861\(98\)00050-9](https://doi.org/10.1016/S0920-5861(98)00050-9).
- [54] M. Lykaki, E. Pachatouridou, E. Iliopoulou, S.A.C. Carabineiro, M. Konsolakis, Impact of the synthesis parameters on the solid state properties and the CO oxidation performance of ceria nanoparticles, *RSC Adv.* 7 (2017) 6160–6169, <https://doi.org/10.1039/C6RA26712B>.
- [55] M. Piumetti, T. Andana, S. Bensaid, N. Russo, D. Fino, R. Pirone, Study on the CO oxidation over ceria-based nanocatalysts, *Nanoscale Res. Lett.* 11 (2016) 165, <https://doi.org/10.1186/s11671-016-1375-z>.
- [56] X. Zhang, F. Hou, Y. Yang, Y. Wang, N. Liu, D. Chen, Y. Yang, A facile synthesis for cauliflower like CeO<sub>2</sub> catalysts from Ce-BTC precursor and their catalytic performance for CO oxidation, *Appl. Surf. Sci.* 423 (2017) 771–779, <https://doi.org/10.1016/j.apsusc.2017.06.235>.
- [57] O.S. Bezkrvnyy, P. Kraszkiewicz, M. Ptak, L. Kepinski, Thermally induced reconstruction of ceria nanocubes into zigzag {111}-nanofaceted structures and its influence on catalytic activity in CO oxidation, *Catal. Commun.* (2018), <https://doi.org/10.1016/j.catcom.2018.08.005>.
- [58] V. Shapovalov, H. Metiu, Catalysis by doped oxides: CO oxidation by AuxCe<sub>1-x</sub>O<sub>2</sub>, *J. Catal.* 245 (2007) 205–214, <https://doi.org/10.1016/j.jcat.2006.10.009>.
- [59] A. Trovarelli, J. Llorca, Ceria catalysts at nanoscale: how do crystal shapes shape catalysis? *ACS Catal.* 7 (2017) 4716–4735, <https://doi.org/10.1021/acscatal.7b01246>.
- [60] A. Trovarelli, C. de Leitenburg, M. Boaro, G. Dolcetti, The utilization of ceria in industrial catalysis, *Catal. Today* 50 (1999) 353–367, [https://doi.org/10.1016/S0920-5861\(98\)00515-X](https://doi.org/10.1016/S0920-5861(98)00515-X).
- [61] E. Aneggi, D. Wiater, C. de Leitenburg, J. Llorca, A. Trovarelli, Shape-dependent activity of ceria in soot combustion, *ACS Catal.* 4 (2013) 172–181, <https://doi.org/10.1021/cs400850r>.
- [62] T.R. Reina, S. Ivanova, O.H. Laguna, M.A. Centeno, J.A. Odriozola, WGS and CO-PrOx reactions using gold promoted copper-ceria catalysts: “Bulk CuO/CeO<sub>2</sub> vs. CuO/CeO<sub>2</sub>/Al<sub>2</sub>O<sub>3</sub> with low mixed oxide content,” *Appl. Catal. B-Environ.* 197 (2016) 62–72, <https://doi.org/10.1016/j.apcatb.2016.03.022>.
- [63] P. Boldrin, E. Ruiz-Trejo, J. Mermelstein, J.M. Bermúdez Menéndez, T. Ramírez Reina, N.P. Brandon, Strategies for carbon and sulfur tolerant solid oxide fuel cell materials, incorporating lessons from heterogeneous catalysis, *Chem. Rev.* 116 (2016) 13633–13684, <https://doi.org/10.1021/acs.chemrev.6b00284>.
- [64] M. Usman, W.W. Daud, H.F. Abbas, Dry reforming of methane: influence of process parameters—a review, *Renew. Sustain. Energy Rev.* 45 (2015) 710–744, <https://doi.org/10.1016/j.rser.2015.02.026>.
- [65] T.E. Bell, G. Zhan, K. Wu, H.C. Zeng, L. Torrente-Murciano, Modification of ammonia decomposition activity of ruthenium nanoparticles by N-doping of CNT supports, *Top Catal.* 60 (2017) 1251–1259, <https://doi.org/10.1007/s11244-017-0806-0>.
- [66] L. Torrente-Murciano, The importance of particle-support interaction on particle size determination by gas chemisorption, *J. Nanopart. Res.* 18 (2016), <https://doi.org/10.1007/s11051-016-3385-2>.
- [67] A.M. Diskin, R.H. Cunningham, R.M. Ormerod, The oxidative chemistry of methane over supported nickel catalysts, *Catal. Today* 46 (1998) 147–154, [https://doi.org/10.1016/S0920-5861\(98\)00336-8](https://doi.org/10.1016/S0920-5861(98)00336-8).
- [68] S.J.A. Livermore, J.W. Cotton, R.M. Ormerod, Fuel reforming and electrical performance studies in intermediate temperature ceria-gadolinia-based SOFCs, *J. Power Sources* 86 (2000) 411–416, [https://doi.org/10.1016/S0378-7753\(99\)00493-0](https://doi.org/10.1016/S0378-7753(99)00493-0).
- [69] J. Guo, H. Lou, H. Zhao, D. Chai, X. Zheng, Dry reforming of methane over nickel catalysts supported on magnesium aluminate spinels, *Appl. Catal. A-Gen.* 273 (2004) 75–82, <https://doi.org/10.1016/j.apcata.2004.06.014>.
- [70] J.M. Rynkowski, T. Paryjczak, M. Lenik, On the nature of oxidic nickel phases in NiO<sub>y</sub>-Al<sub>2</sub>O<sub>3</sub> catalysts, *Appl. Catal. A-Gen.* 106 (1993) 73–82, [https://doi.org/10.1016/0926-860X\(93\)80156-K](https://doi.org/10.1016/0926-860X(93)80156-K).
- [71] M. Li, H. Amari, A.C. van Veen, Metal-oxide interaction enhanced CO<sub>2</sub> activation in methanation over ceria supported nickel nanocrystallites, *Appl. Catal. B: Environ.* 239 (2018) 27–35, <https://doi.org/10.1016/j.apcatb.2018.07.074>.
- [72] A. Vita, C. Italiano, C. Fabiano, M. Laganà, L. Pino, Influence of ce-precursor and fuel on structure and catalytic activity of combustion synthesized Ni/CeO<sub>2</sub> catalysts for biogas oxidative steam reforming, *Mater. Chem. Phys.* 163 (2015) 337–347, <https://doi.org/10.1016/j.matchemphys.2015.07.048>.
- [73] Y. Zhou, J.M. Perket, A.B. Crooks, J. Zhou, Effect of ceria support on the structure of Ni nanoparticles, *J. Phys. Chem. Lett.* 1 (2010) 1447–1453, <https://doi.org/10.1021/jz1003044>.
- [74] M. Bäumer, H.-J. Freund, Metal deposits on well-ordered oxide films, *Prog. Surf. Sci.* 61 (1999) 127–198, [https://doi.org/10.1016/S0079-6816\(99\)00012-X](https://doi.org/10.1016/S0079-6816(99)00012-X).
- [75] T. Stroud, T.J. Smith, E. Le Saché, J.L. Santos, M.A. Centeno, H. Arellano-García, J.A. Odriozola, T.R. Reina, Chemical CO<sub>2</sub> recycling via dry and bi reforming of methane using Ni-Sn/Al<sub>2</sub>O<sub>3</sub> and Ni-Sn/CeO<sub>2</sub>-Al<sub>2</sub>O<sub>3</sub> catalysts, *Appl. Catal. B-Environ.* 224 (2018) 125–135, <https://doi.org/10.1016/j.apcatb.2017.10.047>.
- [76] Y. Wang, L. Yao, S. Wang, D. Mao, C. Hu, Low-temperature catalytic CO<sub>2</sub> dry reforming of methane on Ni-based catalysts: a review, *Fuel Process. Technol.* 169 (2018) 199–206, <https://doi.org/10.1016/j.fuproc.2017.10.007>.
- [77] X. Lv, J.-F. Chen, Y. Tan, Y. Zhang, A highly dispersed nickel supported catalyst for dry reforming of methane, *Catal. Commun.* 20 (2012) 6–11, <https://doi.org/10.1016/j.catcom.2012.01.002>.
- [78] C. Liu, J. Ye, J. Jiang, Y. Pan, Progresses in the preparation of coke resistant Ni-based catalyst for steam and CO<sub>2</sub> reforming of methane, *ChemCatChem* 3 (2011) 529–541, <https://doi.org/10.1002/cctc.201000358>.
- [79] A. Albarazi, M.E. Gálvez, P. Da Costa, Synthesis strategies of ceria-zirconia doped Ni/SBA-15 catalysts for methane dry reforming, *Catal. Commun.* 59 (2015) 108–112, <https://doi.org/10.1016/j.catcom.2014.09.050>.
- [80] J.-M. Lavoie, Review on dry reforming of methane, a potentially more environmentally-friendly approach to the increasing natural gas exploitation, *Front. Chem.* 2 (2014), <https://doi.org/10.3389/fchem.2014.00081>.
- [81] A. Horváth, G. Stefler, O. Geszti, A. Kienneman, A. Pietraszek, L. Guzzi, Methane dry reforming with CO<sub>2</sub> on CeZr-oxide supported Ni, NiRh and NiCo catalysts prepared by sol-gel technique: relationship between activity and coke formation, *Catal. Today* 169 (2011) 102–111, <https://doi.org/10.1016/j.cattod.2010.08.004>.
- [82] A.R. McFarlane, I.P. Silverwood, R. Warringham, E.L. Norris, R.M. Ormerod, C.D. Frost, S.F. Parker, D. Lennon, The application of inelastic neutron scattering to investigate the ‘dry’ reforming of methane over an alumina-supported nickel catalyst operating under conditions where filamentous carbon formation is prevalent, *RSC Adv.* 3 (2013) 16577–16589, <https://doi.org/10.1039/C3RA42435A>.
- [83] T. Margossian, K. Larmier, S.M. Kim, F. Krumeich, A. Fedorov, P. Chen, C.R. Müller, C. Copéret, Molecularly tailored nickel precursor and support yield a stable methane dry reforming catalyst with superior metal utilization, *J. Am. Chem. Soc.* 139 (2017) 6919–6927, <https://doi.org/10.1021/jacs.7b01625>.